

¹ Global ghost imaging

² Nixi Zhao,^{1,2,3} Changzhe Zhao,^{1,2,3} Jie Tang,^{1,2,3} Jianwen Wu,^{1,2,3}
³ Haipeng Zhang,² Han Guo², and TiQiao Xiao^{1,2,3,*}

⁴ *¹Shanghai Institute of Applied Physics, Chinese Academy of Sciences, Shanghai 201800, People's Republic of China*

⁶ *²Shanghai Synchrotron Radiation Facility/Zhangjiang Lab, Shanghai Advanced Research Institute, Chinese Academy of Sciences, Shanghai 201204, People's Republic of China*

⁸ *³University of Chinese Academy of Sciences, Beijing 100049, People's Republic of China*

⁹ *tqiao@sari.ac.cn*

¹⁰ Abstract: Ghost imaging (GI), as a novel imaging technique, offers significant potential com-
¹¹ pared to standard imaging. However, the inability to achieve large field of view, high-resolution,
¹² and high-quality image reconstruction within a short time frame and with a limited number of
¹³ measurements severely hampers the practical application of ghost imaging. We propose global
¹⁴ ghost imaging(GGI) to try to solve the above problems to realize the practicality of ghost imag-
¹⁵ ing. Global ghost imaging executes hundreds of ghost imaging as subsystems at the same time.
¹⁶ Many bucket detectors are placed in the object arm to form an array, and position sensitive de-
¹⁷ tectors are placed in the corresponding positions in the reference arm. Then, a prior knowledge
¹⁸ is introduced, but instead of calculating independently within each local system, the global prior
¹⁹ is used to cover all subsystems. The speckle patterns of each ghost imaging subsystem are up-
²⁰ loaded to the terminal for unified iterative operation, so that the iterative sparse solution of each
²¹ subsystem changes from local optimization to global optimization. Simulation and experiments
²² show that the global ghost imaging can achieve large field of view and high-resolution imaging,
²³ completely eliminate the discontinuity between subsystems, greatly improve the image quality,
²⁴ have strong noise robustness ability, and more importantly, it can achieve image reconstruction
²⁵ with ultra-low number of measurements. Using the classical ghost imaging framework and the
²⁶ computational ghost imaging framework respectively, we show that this method has the ability
²⁷ to reconstruct complex samples with 800×280 pixels in only 8 measurements.

²⁸ 1. Introduction

²⁹ Ghost imaging(GI), i.e. correlation imaging, is a new type of imaging technology based on the
³⁰ correlation characteristics of quantum entanglement [1, 2] or classical light field fluctuations
³¹ [3, 4], which can nonlocally obtain the information of the target object through the intensity
³² correlation between the reference arm and the object arm. Ghost imaging provides a method
³³ that is difficult to obtain clear images by conventional means, and can solve some problems
³⁴ that are not easy to solve by conventional imaging. Ghost imaging has been applied in military,
³⁵ radar detection and optical encryption. It can also be further applied in pathological analysis,
³⁶ material research, life science and material science in the future. GI has been proved to be
³⁷ suitable for classical thermal light sources [3, 4]. Furthermore, it has also been proved to be
³⁸ suitable for atoms [5], electrons [6], neutrons [7, 8] and X-ray [9–13]. Computational ghost
³⁹ imaging (CGI) [14] uses a spatial light modulator (SLM) to modulate the light field, eliminating
⁴⁰ the steps of recording structural illumination, thus forming a system architecture consistent with
⁴¹ single pixel imaging (SPI).

⁴² However, ghost imaging requires thousands of measurements to reconstruct a large field of
⁴³ view and high-resolution image, and each acquisition requires a completely different mask to be
⁴⁴ replaced, both of which are time-consuming. Many measurements and long experimental time
⁴⁵ have caused serious difficulties for the practical application of ghost imaging. It may take tens of
⁴⁶ thousands of measurements to reconstruct a result with 256×256 pixels and take several hours
⁴⁷ or even longer. In order to solve this problem, various ghost imaging technologies try to mine

48 the information buried in the dual arm signal from various dimensions to reduce the number of
 49 measurements required to reconstruct high-quality images. Reconstruction algorithms can be di-
 50 vided into three categories according to the type of iteration, including linear non iterative meth-
 51 ods (e.g. traditional ghost imaging (TGI), differential ghost imaging(DGI) [15] and normalized
 52 ghost imaging(NGI) [16]), linear iterative methods (e.g. gradient descent-GD) and nonlinear
 53 iterative methods (e.g. total variation augmented Lagrangian alternative direction algorithm-
 54 TVAL3 [17]). By adding light intensity fluctuation correction, digital mask sorting [18, 19] and
 55 compressed sensing [20, 21] and other methods, the existing GI methods have made full use
 56 of the object information contained in each pixel, and it seems difficult to further reduce the
 57 number of measurements required for high-quality imaging without changing the experimental
 58 architecture.

59 Here, we propose global ghost imaging (GGI) from the perspective of convex optimization.
 60 This method is no longer confined to the information inside the local system. Hundreds of bucket
 61 detectors are placed close to each other in the object arm to form an array, and hundreds of ghost
 62 imaging measurements are performed at the same time. The information of various dimensions
 63 and each iteration in each subsystem are shared and coordinated globally. In each iteration of
 64 each ghost imaging subsystem, not only the object information in the subsystem is the source, but
 65 the results of all subsystems in the global domain of the previous iteration are used as a reference
 66 to jointly find the gradient statistical sparse optimal solution of the sample image globally, so that
 67 each ghost imaging subsystem is no longer in the local optimal trap. This method not only greatly
 68 improves the image quality, but also reduces the noise of the reconstruction results. Since the
 69 ghost imaging subsystems share the same regularization prior globally, the strong discontinuity
 70 at the junction of each subsystem is no longer generated from the underlying mechanism. The
 71 prior unification in the global domain and the interactive iterative operation between subsystems
 72 further significantly reduce the number of sampling required for high-quality imaging. Simula-
 73 tion and experiments using classical ghost imaging framework [22–26] and computational ghost
 74 imaging framework [27] verify the ability of this method to reconstruct complex samples with
 75 280×800 pixels in only 8 measurements. This will greatly reduce the dose required for X-ray
 76 imaging, and shorten the whole experimental process to 10 seconds or so. Computational ghost
 77 imaging framework can save the time-consuming reference arm recording process, which can
 78 further reduce the total experimental time by more than half. We believe that this research will
 79 provide a new framework for ghost imaging, which will greatly promote the practical process of
 80 ghost imaging.

81 2. Principle, universal interface and simulation experiment

82 In the framework of global ghost imaging experiment, each ghost imaging subsystem can be
 83 simply written as a linear system:

$$\begin{bmatrix} b_1 \\ b_2 \\ \vdots \\ b_n \end{bmatrix} = \begin{bmatrix} A(1,1) & A(1,2) & \cdots & A(1,m) \\ A(2,1) & A(2,2) & \cdots & A(2,m) \\ \vdots & \vdots & \ddots & \vdots \\ A(n,1) & A(n,2) & \cdots & A(n,m) \end{bmatrix} \begin{bmatrix} x_1 \\ x_2 \\ \vdots \\ x_m \end{bmatrix} \quad (1)$$

84 Where $A \in R^{n \times m}$ is the mask modulation matrix, that is, the speckle pattern. $x \in R^{m \times 1}$ is the
 85 object image, which is the unknown variable we need to solve. $b \in R^{n \times 1}$ is the bucket detection
 86 signal sequence. m is the number of image pixels and n is the number of measurements. This
 87 subsystem can be abbreviated as $Ax = b$. The essence of ghost imaging is to solve a system of
 88 underdetermined linear equations. All ghost imaging methods are committed to mining the

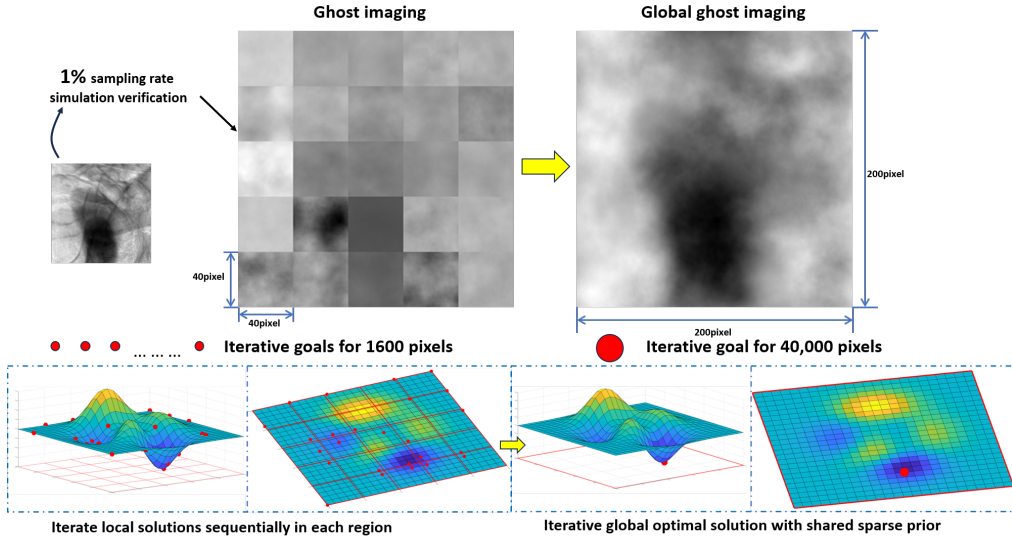


Fig. 1. Schematic diagram of global ghost imaging principle; modifying GI algorithm to implement GGI.

89 information of objects from the modulated light field A and single pixel signal b as much as
90 possible. In global ghost imaging, hundreds of bucket detectors are placed close to each other
91 on the object arm, and the imaging process can be written as follows:

$$\begin{aligned}
A_{1,1}x_{1,1} &= b_{1,1}; A_{1,2}x_{1,2} = b_{1,2}; \dots; A_{1,M}x_{1,M} = b_{1,M}, \\
A_{2,1}x_{2,1} &= b_{2,1}; A_{2,2}x_{2,2} = b_{2,2}; \dots; A_{2,M}x_{2,M} = b_{2,M}, \\
&\dots \\
A_{N,1}x_{N,1} &= b_{N,1}; A_{N,2}x_{N,2} = b_{N,2}; \dots; A_{N,M}x_{N,M} = b_{N,M}
\end{aligned} \tag{2}$$

92 The unknown variable of global ghost imaging, X , consists of $x_{1,1}, x_{1,2}, \dots, x_{n,m}$ and is a vector
93 in ultra-high dimensional space. This framework makes it possible for GGI to reconstruct large
94 field of view results with very low measurements.

95 The schematic diagram of the principle of global ghost imaging is shown in Fig.1. This
96 method is a concept and is not restricted to a specific algorithm. However, due to the unique
97 bucket detector array framework of GGI, the ghost imaging algorithm cannot be directly adapted.
98 We take TVAL3 as an example to show the principle of GGI and the method of converting GI
99 algorithm to GGI. TVAL3 is a nonlinear iterative algorithm based on compressed sensing, which
100 can be simply expressed as:

$$\begin{aligned}
&\text{Min}||c||_{l_0} \\
&\text{s.t. } Dx = c; \\
&\quad Ax = b
\end{aligned} \tag{3}$$

101 $Ax = b$ is the measurement model of ghost imaging, D is the conversion matrix, converting the
102 object image x to c , l_0 norm calculates the number of non-zero elements in c and minimizes
103 this index to find sparse solutions. The l_0 norm is a non-convex function and is difficult to solve.
104 It is usually approximated by the l_1 norm. TVAL3 requires fewer iterations, has strong noise
105 robustness and high reconstructed image quality. It is one of the most powerful ghost imaging

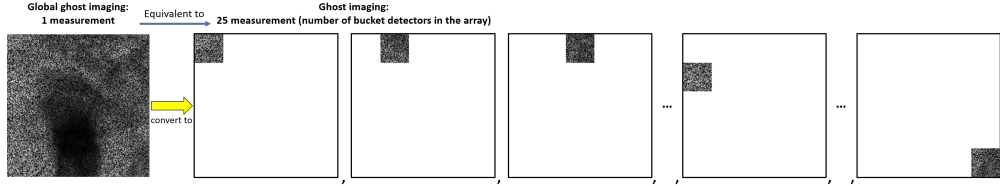


Fig. 2. More general GGI interface; reverse conversion of GGI speckle pattern to GI form

106 algorithms at present and has withstood the test of numerous experiments. When modified into
 107 a global algorithm, TVAL3 can be expressed as:

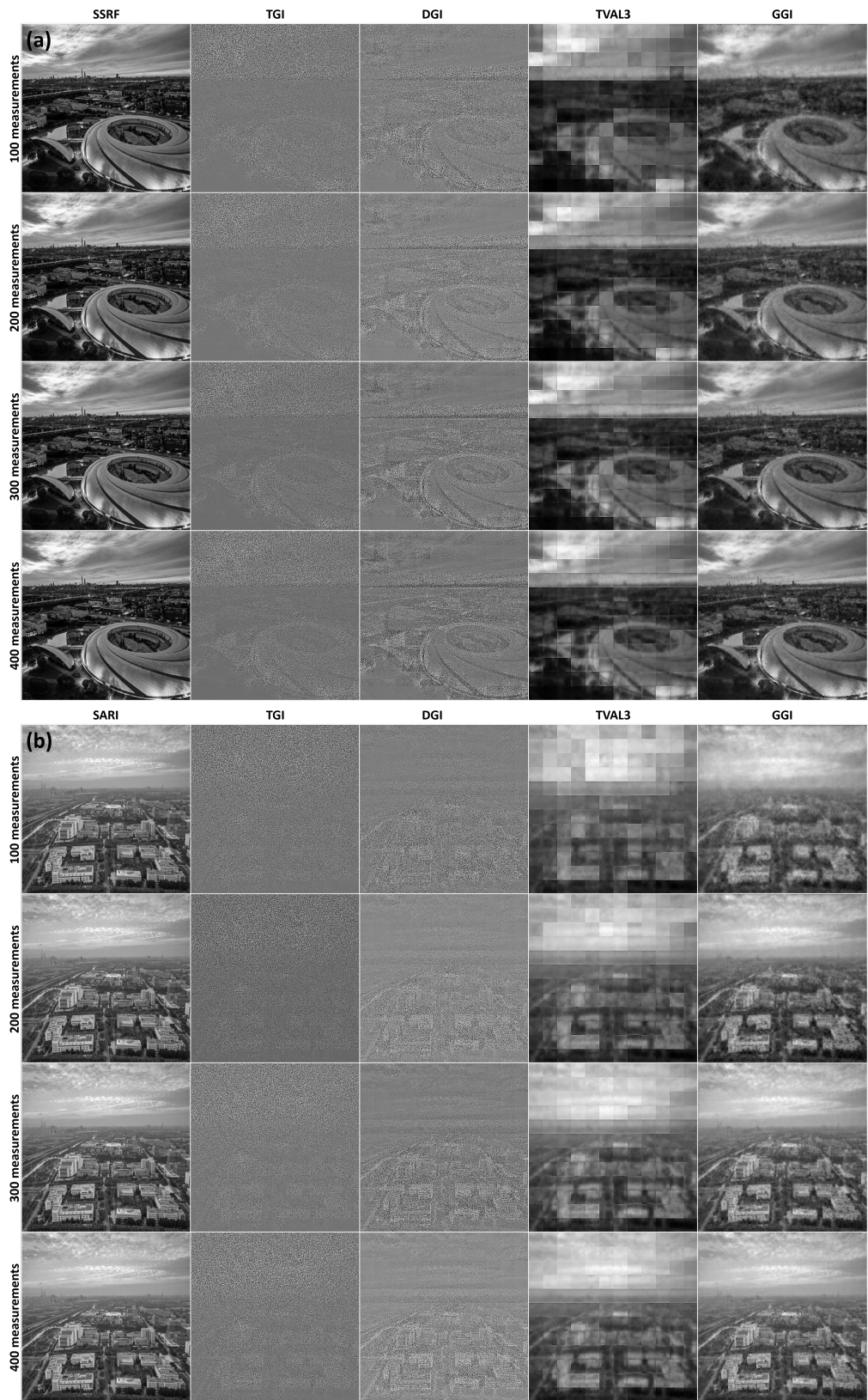
$$\begin{aligned}
 & \text{Min} ||C||_0 \\
 & \text{s.t. } DX = C; \\
 & A_{1,1}x_{1,1} = b_{1,1}; \\
 & A_{1,2}x_{1,2} = b_{1,2}; \\
 & \quad \cdots; \\
 & A_{1,M}x_{1,M} = b_{1,M}; \\
 & \quad \cdots; \\
 & A_{N,M}x_{N,M} = b_{N,M};
 \end{aligned} \tag{4}$$

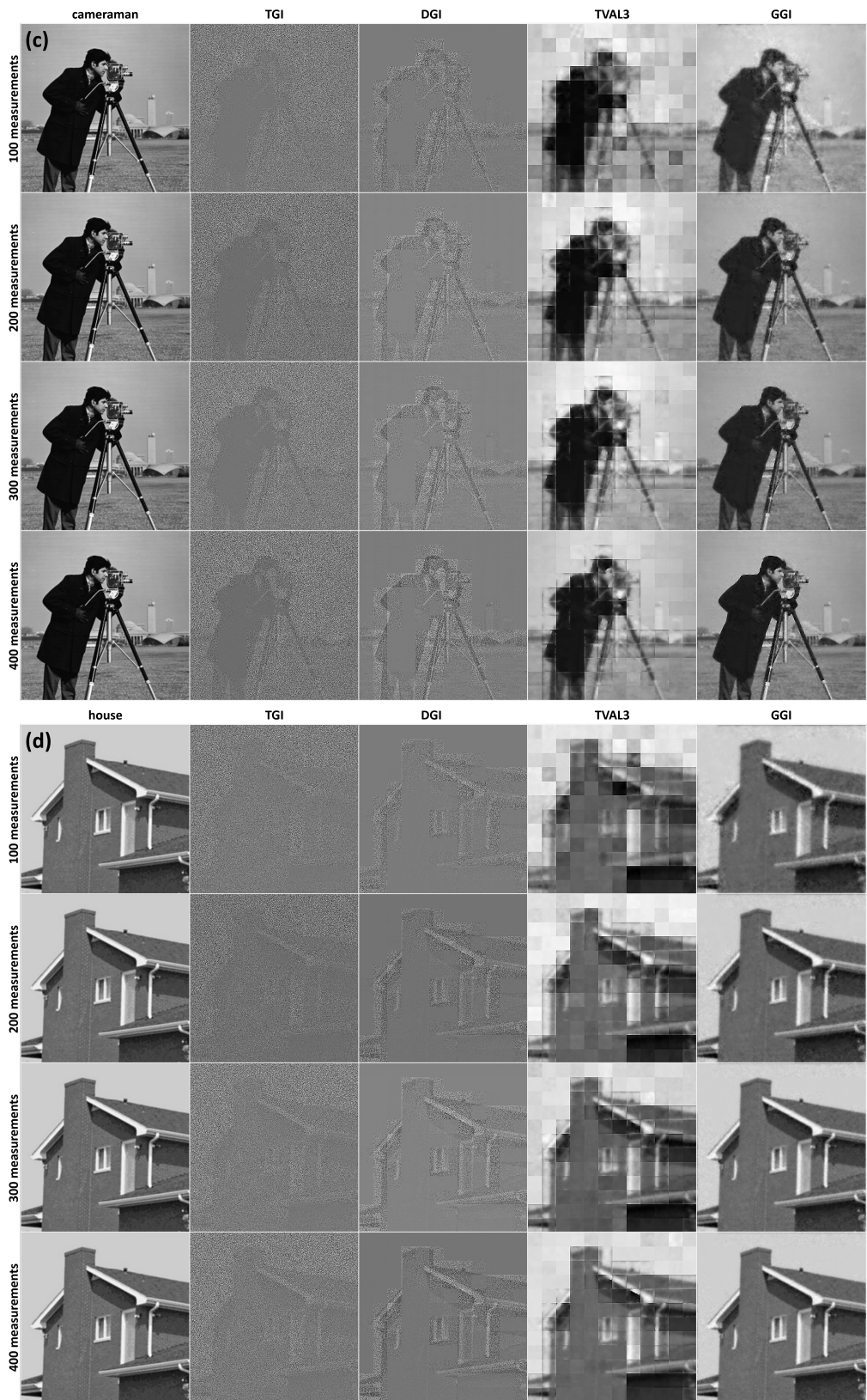
108 As mentioned in GGI imaging process, X is a huge variable to be solved consisting of $x_{1,1}, x_{1,2}, \dots, x_{N,M}$.
 109 Global ghost imaging adds hundreds of ghost imaging subsystem sampling processes to the limit
 110 equation, and only uses the same prior knowledge to iterate X as a whole. The Augmented La-
 111 grange method will throw $N \times M$ constraint equations onto the iteration target, so that the whole
 112 is transformed into an unrestricted equation. This is an ultra long iteration goal with many vari-
 113 ables, which requires a large memory space for the computer.

114 Global ghost imaging liberates each ghost imaging subsystem from the local optimal itera-
 115 tion trap, and jointly iterates to find the global optimal solution. Global ghost imaging shows
 116 powerful performance, which is stronger than all existing ghost imaging methods. We will make
 117 extensive comparison and prove this later. However, GGI still has a small problem hindering
 118 its wide application - every GI algorithm needs to be rewritten to adapt to the GGI architec-
 119 ture, which is annoying and time-consuming. To address this, we propose a reverse conversion
 120 method that convert the speckle patterns of GGI into GI adapted form, which is more efficient
 121 than previously adapting GI algorithms to GGI.

122 The schematic diagram of the reverse conversion from global ghost imaging to ghost imaging
 123 is shown in Fig.2. One measurement of global ghost imaging can be equivalent converted to
 124 $N \times M$ measurements of ghost imaging. The number of measurements increases hundreds of
 125 times while preserving large field of view, so that any GI algorithm can achieve high-quality
 126 reconstruction with a large field of view and a small number of measurements. This is equivalent
 127 to a measurement number amplification technology, which provides a universal GGI oriented
 128 interface for all GI algorithms. This will greatly reduce the use threshold of GGI and improve
 129 its versatility.

130 Firstly, the performance of global ghost imaging is detected in the simulation experiment with-
 131 out introducing experimental error. The experimental results of a series of simulated global ghost
 132 imaging are listed in Fig.3.(a-d). The target image size is 480×480 pixels. In the simulation
 133 experiment, 12×12 bucket detectors are placed in the object arm, and the image size of each
 134 ghost imaging subsystem is 40×40 pixels. In order to ensure that the simulation experiment





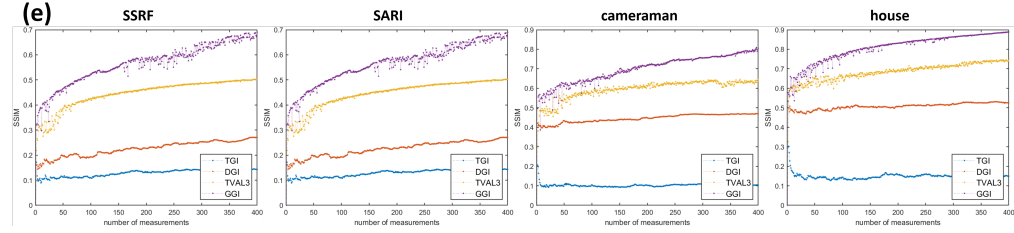


Fig. 3. Comparison of TGI, DGI, TVAL3, and GGI through simulation experiments (image size 480×480). The reconstruction was performed using (a)SSRF, (b)SARI, (c)cameraman, and (d)house as object images with measurements of 100, 200, 300, and 400, respectively.(e)SSIM between TGI, DGI, TVAL3 and GGI.

135 results are not affected by the random distribution fluctuation of speckle pattern, all simulation
 136 experiments use the same group of randomly distributed speckle patterns. The maximum num-
 137 ber of measurements is 400, which means that for the traditional single pixel ghost imaging,
 138 the sampling rate is only 0.17%, which is hardly imageable, so it is no longer included in the
 139 comparison. We will use TGI, DGI and TVAL3 bucket detector array ghost imaging and GGI
 140 for comparison. The measurement numbers are 100, 200, 300 and 400 respectively. SSIM is an
 141 index to evaluate the similarity between reconstruction results and objects. The comparison of
 142 SSIM values of the four methods is shown in Fig 3.e.

143 Because of its low utilization of object information, TGI can only vaguely see the outline of
 144 the object in low sampling image reconstruction. DGI is a variant of TGI, and its effect has been
 145 improved. TVAL3 performs well in low sampling image reconstruction, and can reconstruct
 146 the object details in a single subsystem at 200 measurements. However, due to the introduction
 147 of priori in each local system, the image fragmentation caused by the discontinuity between
 148 subsystems is extremely serious. Especially in image reconstruction with a lower number of
 149 measurements (100), the image is completely torn by discontinuities. Global ghost imaging
 150 overcomes these defects. Without introducing experimental errors, the reconstruction results of
 151 images with large field of view not only have no discontinuities between subsystems, but also
 152 the quality of reconstructed images is much higher than that of TVAL3. At 100 measurements,
 153 even if discontinuities are ignored, the reconstruction of TVAL3 in a single subsystem is almost
 154 fail. Global ghost imaging has completed the task well, and its limit is far more than that. We
 155 will discuss it again later. The SSIM value of GGI from 2 to 400 measurements is much higher
 156 than that of other methods, which strongly supports the above statement.

157 3. Experimental setup, speckle analysis, experimental results and reconstruction of
 158 ultra-low measurement number

159 In response to the demand for beam splitting in X-ray ghost imaging, we have built a crystal beam
 160 splitting system at the X-ray testing line station BL09B [28] of Shanghai Synchrotron Radiation
 161 Facility (SSRF) to achieve global ghost imaging in a classical framework. To achieve high-
 162 quality spatial intensity correlation beam splitting, we have developed a crystal beam splitter [22–
 163 26] specifically designed for XGI. The beam splitter is a 300 μm thick Laue diffraction crystal
 164 developed, with a diffraction Bragg angle of 5.67°. The photon energy during the experiment is
 165 20keV. X-rays pass through the copper foam to create a speckle pattern. The splitter divides the
 166 modulated beam into two beams in the reference arm and the object arm, with an intensity ratio
 167 of 16:1. The developed beam splitter can achieve beam splitting with a large field of view, and
 168 the beam splitting correlation can reach 0.9 or above. The position sensitive detector (Onsemi
 169 KAI-16000) will simultaneously record two beams, with the weaker beam being manually fitted

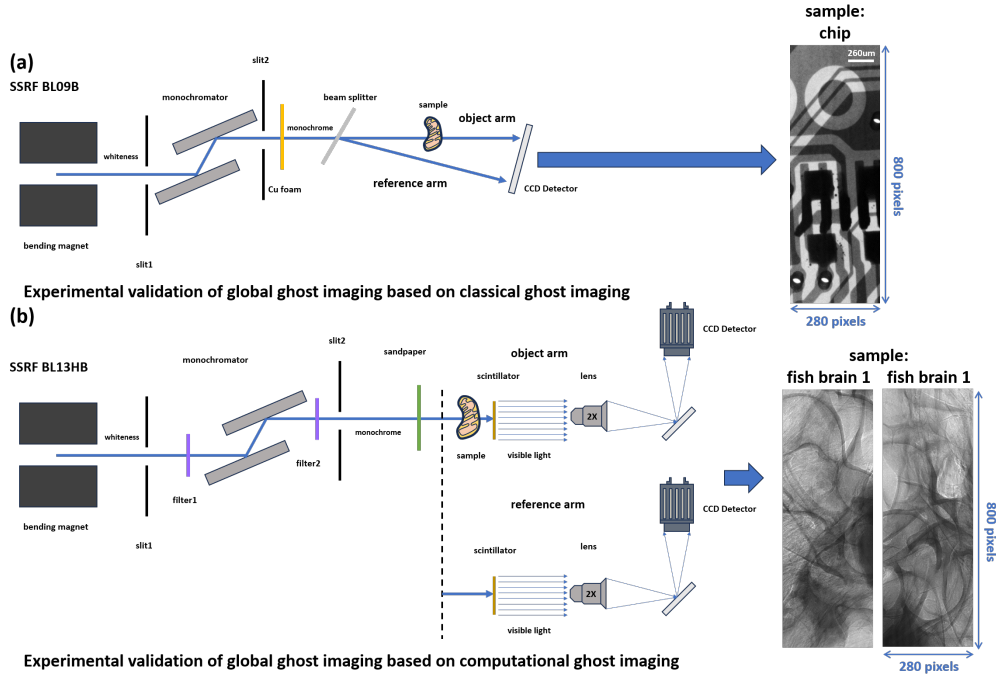


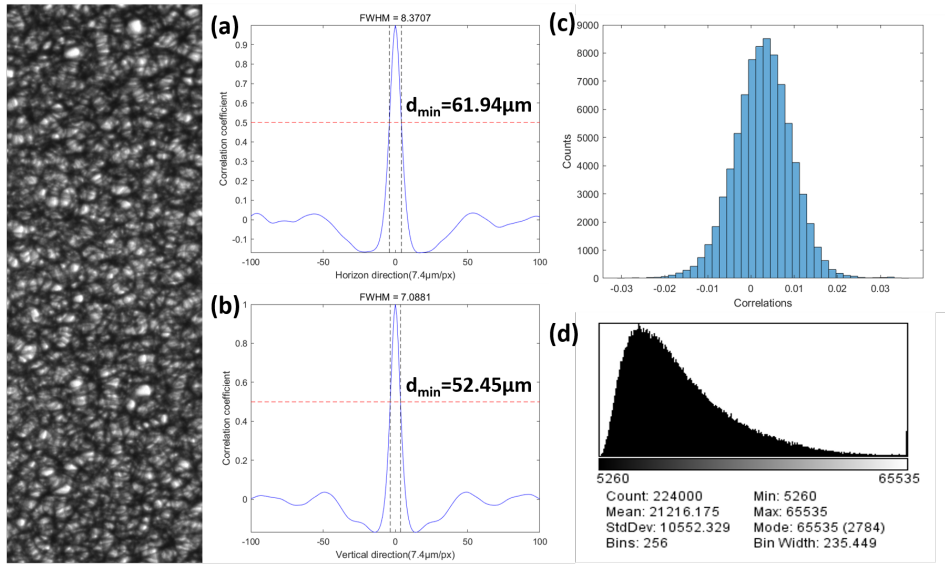
Fig. 4. (a)Experimental platform for GGI based on classic ghost imaging framework at BL09B. (b)Experimental platform for GGI based on computational ghost imaging framework at BL13H B.

170 into a bucket detector array. The effective area of the CCD detector is $36 \times 24\text{mm}^2$, with a pixel
 171 size of $7.4 \mu\text{m}$. The schematic diagram of the experimental setup is shown in Fig.4.(a) .

172 In order to more systematically and comprehensively verify the performance of global ghost
 173 imaging, we also built a virtual beam splitting system at the X-ray imaging and biomedical appli-
 174 cation beamline BL13HB [29] of SSRF to achieve global ghost imaging within the framework
 175 of computational ghost imaging. The modulator consists of 7 layers of 200 mesh sandpaper, and
 176 the motor carrying the sample moves in and out the beam to record the object arm and reference
 177 arm. The bucket detector array is also artificially fitted. The photon energy during the experi-
 178 ment was 15keV. The imaging system consists of a 100μm thick scintillation crystal (LuAG: Ce),
 179 an optical conversion microscope (model: Optique Peter MICRX016), and an sCMOS detector
 180 (Hamamatsu ORCA Flash 4.0 C11440). The effective area of the detector is $6.6 \times 6.6\text{mm}^2$, with
 181 a pixel size of $3.25 \mu\text{m}$. The experimental setup is shown in Fig.4.(b) .

182 Because the resolution of the reconstruction results cannot be smaller than the minimum effec-
 183 tive features of speckle patterns, speckle patterns have a decisive impact on the reconstruction
 184 quality of ghost imaging, quantification and discussion of them are necessary. For classical
 185 ghost imaging, the thickness of modulator foam copper is about $300 \mu\text{m}$, the aperture is between
 186 $150 \mu\text{m}$ and $190 \mu\text{m}$, and the average voidage is about 77.4%. The full width at half maximum
 187 (FWHM) of the point spread function (PSF) is $61.94 \mu\text{m}$ horizontally (Fig.5.(a)) and $52.45 \mu\text{m}$
 188 vertically (Fig.5.(b)). For calculating ghost imaging, the hole size of the modulator sandpaper
 189 is $70 \mu\text{m}$, and the FWHM of PSF is $29.23 \mu\text{m}$ in the horizontal direction (Fig.5.(e)) and $29.45 \mu\text{m}$
 190 in the vertical direction (Fig.5.(f)). The X-ray modulation capabilities of the above two are
 191 shown in Fig (d) And (h), the modulation ability of copper foam is stronger. The minimum effec-
 192 tive characteristic of sandpaper is smaller than that of copper foam, but because the modulation

Speckle patterns of classical ghost imaging-Copper foam



Speckle patterns of computational ghost imaging-Sandpaper

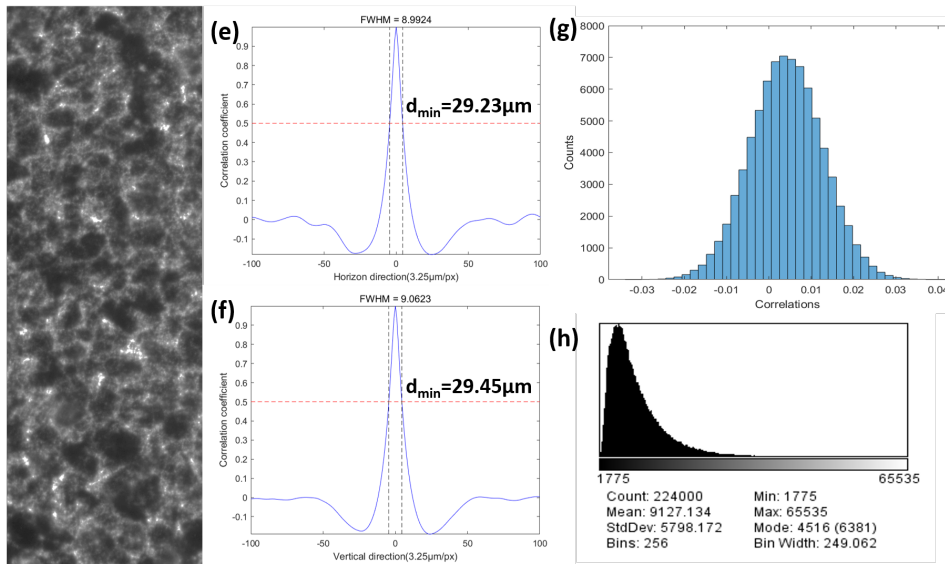


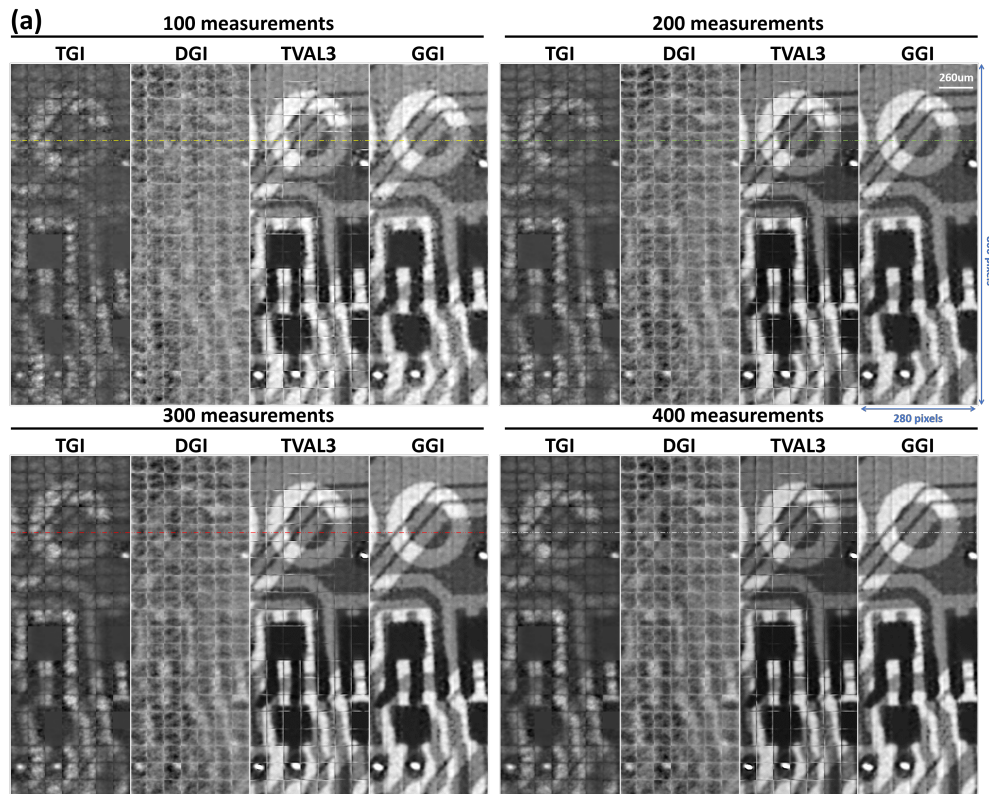
Fig. 5. Speckle analysis—copper foam and sandpaper; The FWHM of PSF in horizontal(a,e) and vertical(b,f) directions; (c,g)Statistical histogram of speckle patterns correlation; (d,h)Statistical histogram of speckle patterns correlation

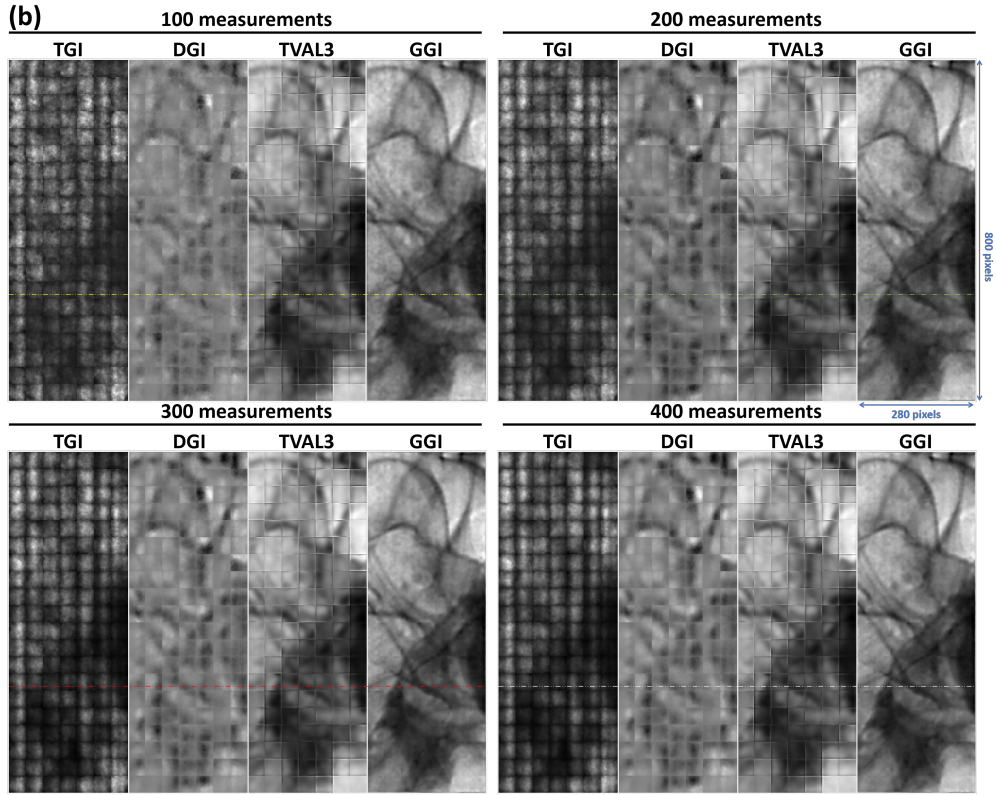
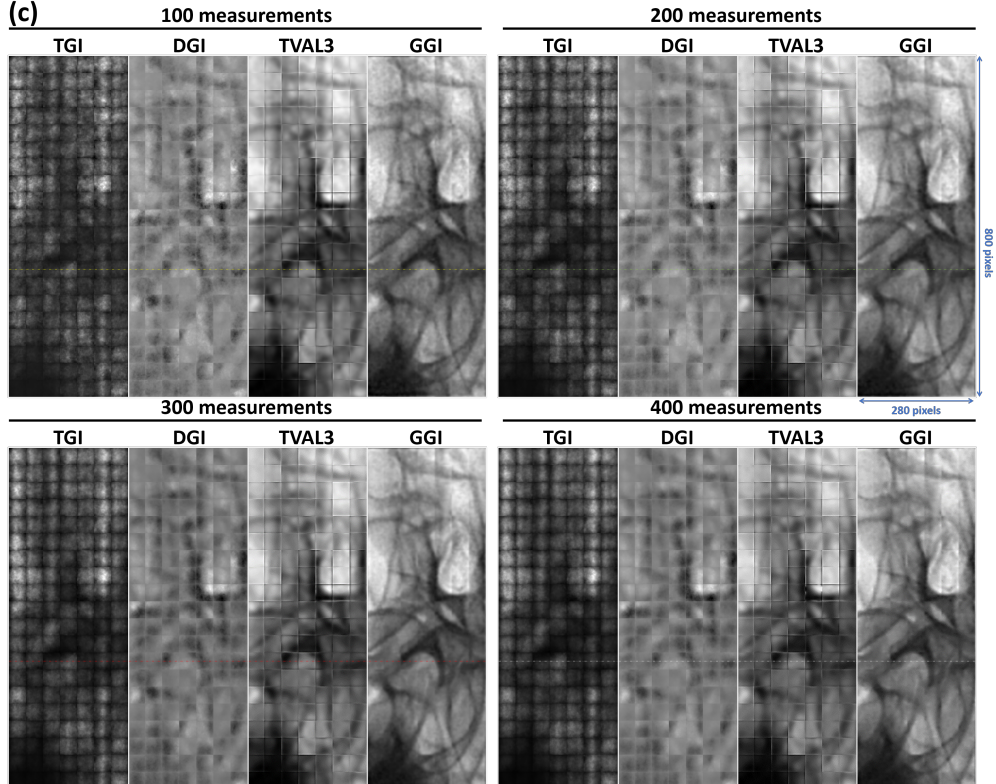
193 ability of sandpaper is weaker, copper foam is more suitable for higher energy experiments.

194 The quality of reconstruction results is also affected by the degree of correlation between
195 speckle patterns. If there are speckles that can be represented by linear superposition of other
196 speckle patterns, it is considered invalid sampling. The statistical histogram of the correlation
197 between any combination of two speckle patterns (C_{400}^2) is shown in Fig (c) And (g), the copper
198 foam is more uncorrelated, and both can approximately regard the random speckle patterns as
199 orthogonal to each other.

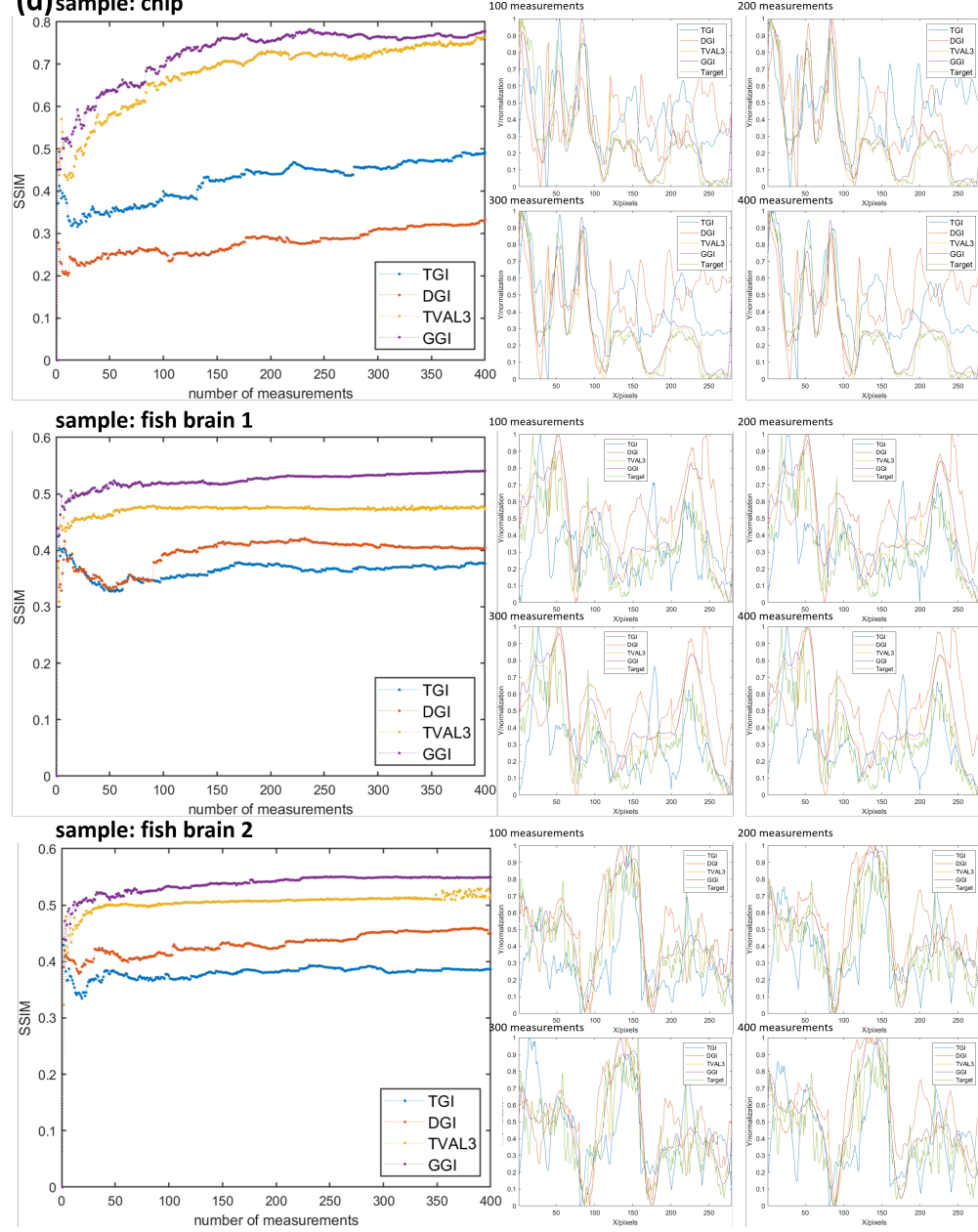
200 In the classic ghost imaging framework, we use chips as sample. In the computational ghost
201 imaging framework, in order to challenge the ultimate ability of global ghost imaging, fish brains
202 with high complexity and low absorption contrast were selected as samples. The object image
203 size is 800×280 pixels, and the image size of a single ghost imaging subsystem is 40×40 pixels.
204 The results of the experimental verification are listed in Fig.6.(a-c), and the comparison graphs
205 of SSIM values and cross-sectional lines with increasing measurement numbers are located in
206 Fig.6.(d). Experimental results have shown that GGI using crystal beam splitting scheme and
207 virtual beam splitting scheme both have higher imaging quality than other methods, without any
208 discontinuity caused by independent measurements between subsystems. This enables ghost
209 imaging to reconstruct large-sized, high-quality, and high-resolution images with fewer samples.

210 An interesting phenomenon was discovered in the experiment. Because of the short wave and
211 strong penetration of X-ray, the beam splitter cannot divide the beam into two identical beams.
212 This means that the speckle patterns of the reference arm and the object arm are not exactly the
213 same in the classical framework, which not only leads to the inconsistency of the FWHM of PSF
214 in Figure a and Figure b, but also results in poorer reconstruction quality of DGI compared to
215 TGI only in experiments with chips as samples.

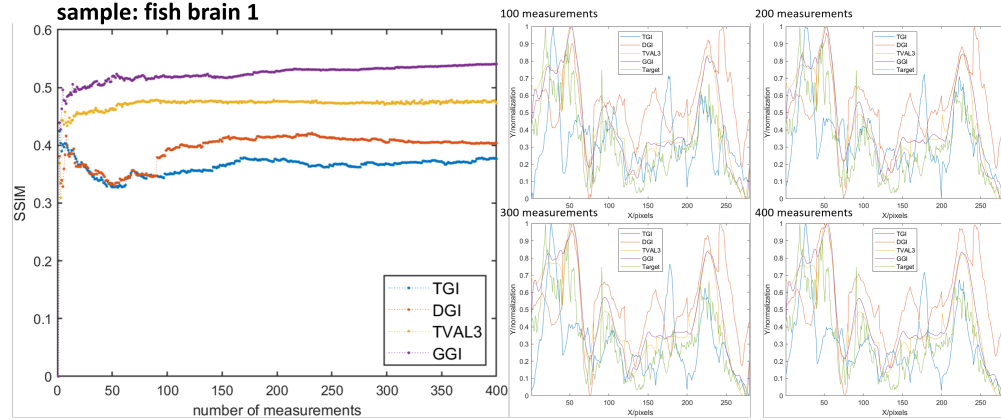


(b)**(c)**

(d) sample: chip



sample: fish brain 1



sample: fish brain 2

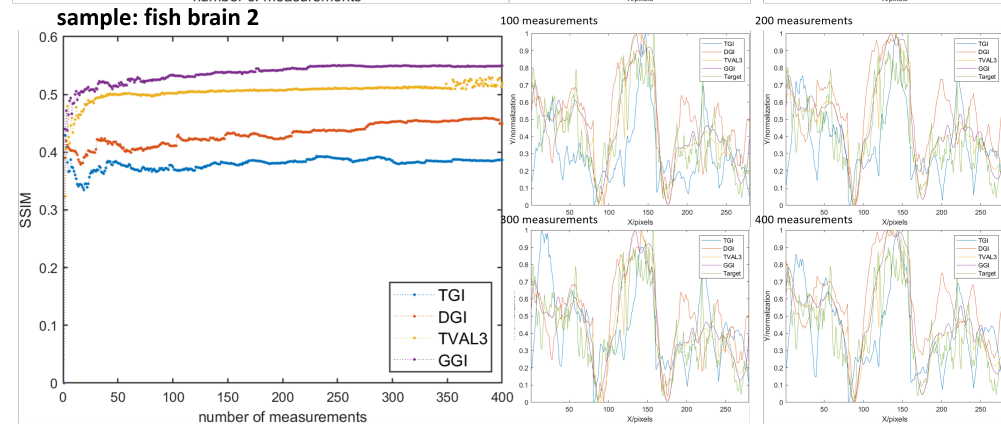
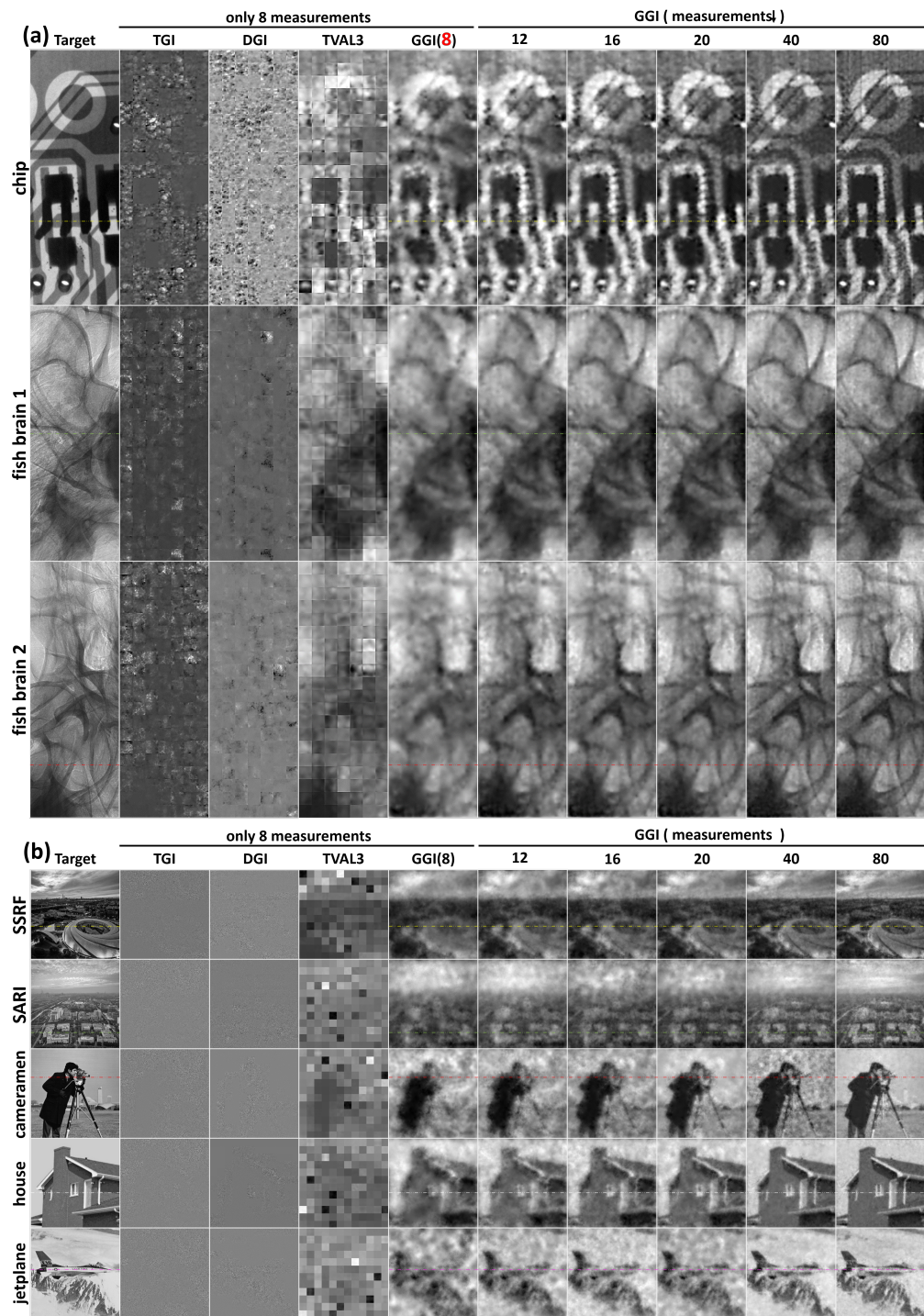


Fig. 6. Comparison of TGI, DGI, TVAL3, and GGI through experiments (image size 280×800). (a)chip, 20keV; (b)fish brain1, 15keV; (c)fish brain2, 15keV; (d)SSIM and cross sectional lines of (a), (b) and (c).



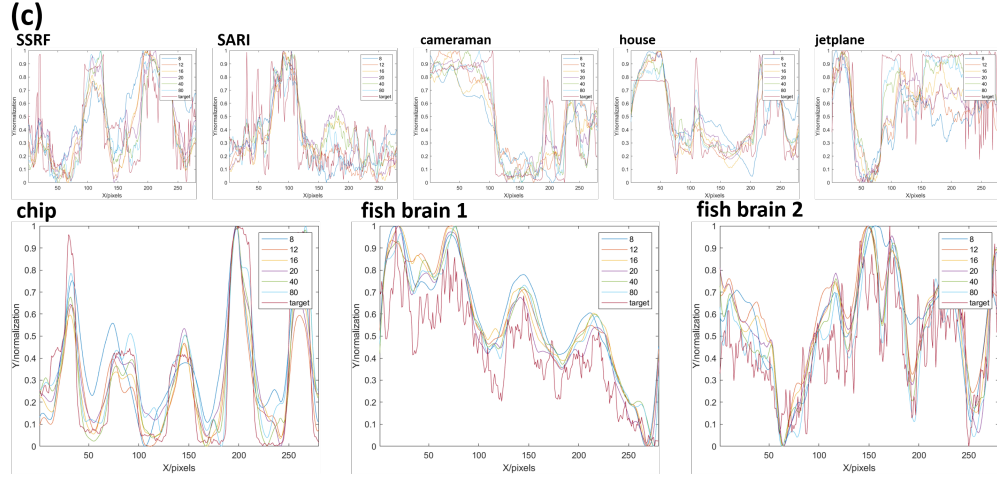


Fig. 7. Reconstruction results of GGI with ultra-low measurements(only 8).
 (a)Experimental results; (b)Simulation results; (c)cross sectional lines

Finally, we demonstrate that GGI can reconstruct high-quality, large field of view results with only 100 measurements. Whether for a subsystem, namely traditional ghost imaging (40×40 , sampling rate 6.25%), or the entire bucket detector array (220×800 , sampling rate 0.000568%), the performance presented by GGI is astonishing. But this is far from the limit of the ability for global ghost imaging. A lower number of measurements means a lower X-ray ionizing radiation dose and a more efficient acquisition process, which has enormous value for the practical application of ghost imaging. So we will further demonstrate the high-quality reconstruction of GGI with ultra-low measurement numbers, as evidenced by Fig.7.

Multiple sets of objects in both experiments and simulation have proven that GGI can still reconstruct object images with only eight measurements! This is an ultra-low measurement count where other ghost imaging techniques have completely failed, or even collapsed. Global ghost imaging provides the conditions for low-dose imaging that is hundreds of times lower than X-ray standard imaging, and is expected to shorten the entire experimental process to within ten seconds or so.

230 4. Conclusion

In conclusion, we propose global ghost imaging method and provide a way to convert conventional GI methods to GGI, as well as a simpler and more universal reverse conversion method to convert the speckle patterns of GGI into GI form. We comprehensively and systematically demonstrate through simulation and experiments that GGI significantly improves the image quality of reconstruction results and eliminates the discontinuity between subsystems. Furthermore, we verify that global ghost imaging can also image large-sized objects at ultra-low sampling rates. This method is highly valuable in the field of medical imaging, and is also feasible for atoms, electrons, and neutrons. It has extremely high practical value, deep scalability, and broad application prospects. We believe that this study provides a new framework for ghost imaging, which will greatly accelerate the practical process of ghost imaging.

Funding. The National Key Research and Development Program of China (Grant Nos. 2022YFA1603601, 2021YFF0601203, 2021YFA1600703), the Young Scientists Fund of the National Natural Science Foundation of China (Grant No.12205361)

Acknowledgment. The authors thank WenJie Hao, Kang Du, Zenghao Song, JunXiong Fang, YanLing

245 Xue, Ke Li and FeiXiang Wang for their kind help and fruitful discussion on experiments and data process-
246 ing.

247 **Disclosures.** The authors declare no conflicts of interest.

248 **Data Availability Statement.** Data underlying the results presented in this paper are not publicly available
249 at this time but may be obtained from the authors upon reasonable request.

250 **References**

1. T. B. Pittman, Y. Shih, D. Strekalov, and A. V. Sergienko, “Optical imaging by means of two-photon quantum entanglement,” *Phys. Rev. A* **52**, R3429 (1995).
2. D. Strekalov, A. Sergienko, D. Klyshko, and Y. Shih, “Observation of two-photon “ghost” interference and diffraction,” *Phys. review letters* **74**, 3600 (1995).
3. R. S. Bennink, S. J. Bentley, and R. W. Boyd, ““two-photon” coincidence imaging with a classical source,” *Phys. review letters* **89**, 113601 (2002).
4. F. Ferri, D. Magatti, A. Gatti, *et al.*, “High-resolution ghost image and ghost diffraction experiments with thermal light,” *Phys. review letters* **94**, 183602 (2005).
5. R. I. Khakimov, B. Henson, D. Shin, *et al.*, “Ghost imaging with atoms,” *Nature* **540**, 100–103 (2016).
6. S. Li, F. Cropp, K. Kabra, *et al.*, “Electron ghost imaging,” *Phys. review letters* **121**, 114801 (2018).
7. A. M. Kingston, G. R. Myers, D. Pelliccia, *et al.*, “Neutron ghost imaging,” *Phys. Rev. A* **101**, 053844 (2020).
8. Y.-H. He, Y.-Y. Huang, Z.-R. Zeng, *et al.*, “Single-pixel imaging with neutrons,” *Sci. Bull.* **66**, 133–138 (2021).
9. H. Yu, R. Lu, S. Han, *et al.*, “Fourier-transform ghost imaging with hard x rays,” *Phys. review letters* **117**, 113901 (2016).
10. D. Pelliccia, A. Rack, M. Scheel, *et al.*, “Experimental x-ray ghost imaging,” *Phys. review letters* **117**, 113902 (2016).
11. A. Schori and S. Shwartz, “X-ray ghost imaging with a laboratory source,” *Opt. express* **25**, 14822–14828 (2017).
12. D. Pelliccia, M. P. Olbinado, A. Rack, *et al.*, “Towards a practical implementation of x-ray ghost imaging with synchrotron light,” *IUCrJ* **5**, 428–438 (2018).
13. A. Schori, D. Borodin, K. Tamasaku, and S. Shwartz, “Ghost imaging with paired x-ray photons,” *Phys. Rev. A* **97**, 063804 (2018).
14. J. H. Shapiro, “Computational ghost imaging,” *Phys. Rev. A—Atomic, Mol. Opt. Phys.* **78**, 061802 (2008).
15. F. Ferri, D. Magatti, L. Lugiato, and A. Gatti, “Differential ghost imaging,” *Phys. review letters* **104**, 253603 (2010).
16. B. Sun, S. S. Welsh, M. P. Edgar, *et al.*, “Normalized ghost imaging,” *Opt. Express* **20**, 16892–16901 (2012).
17. C. Li, W. Yin, H. Jiang, and Y. Zhang, “An efficient augmented lagrangian method with applications to total variation minimization,” *Comput. Optim. Appl.* **56**, 507–530 (2013).
18. Z. Zhou, S.-G. Li, Q.-S. Tan, *et al.*, “Optimization method of hadamard coding plate in γ -ray computational ghost imaging,” *Nucl. Sci. Tech.* **34**, 13 (2023).
19. H. Zhang, K. Du, C. Zhao, *et al.*, “Optimizing the ordering of the hadamard masks of ghost imaging suitable for the efficient face reconstruction using the max-projection method,” *Sci. Reports* **13**, 22702 (2023).
20. D. L. Donoho, “Compressed sensing,” *IEEE Trans. on information theory* **52**, 1289–1306 (2006).
21. H. Zhang, K. Li, C. Zhao, *et al.*, “Efficient implementation of x-ray ghost imaging based on a modified compressive sensing algorithm,” *Chin. Phys. B* **31**, 064202 (2022).
22. Z. Hai-Peng, Z. Chang-Zhe, J. Xiao-Lu, *et al.*, “Improving quality of crystal diffraction based x-ray ghost imaging through iterative reconstruction algorithm br,” *ACTA PHYSICA SINICA* **71** (2022).
23. Z. Chang-Zhe, S. Shang-Yu, Z. Hai-Peng, *et al.*, “Beam splitting characteristics of crystal x-ray laue diffraction,” *ACTA PHYSICA SINICA* **71** (2022).
24. C.-Z. Zhao, S.-Y. Si, Q.-S. Diao, *et al.*, “Development of stress-free laue diffraction crystal for x-ray beam splitting,” in *International Conference on Optical and Photonic Engineering (icOPEN 2023)*, vol. 13069 (SPIE, 2024), pp. 328–334.
25. C.-Z. Zhao, S.-Y. Si, H.-P. Zhang, *et al.*, “Intensity correlation properties of x-ray beams split with laue diffraction,” *Chin. Phys. B* **33**, 014102 (2024).
26. C.-Z. Zhao, H.-P. Zhang, J. Tang, *et al.*, “X-ray ghost imaging with a specially developed beam splitter,” *Synchrotron Radiat.* **31** (2024).
27. H. Zhang, K. Li, F. Wang, *et al.*, “Megapixel x-ray ghost imaging with a binned detector in the object arm,” *Chin. Opt. Lett.* **20**, 033401 (2022).
28. Z. Li, Y. Fan, L. Xue, *et al.*, “The design of the test beamline at ssrf,” in *PROCEEDINGS OF THE 13TH INTERNATIONAL CONFERENCE ON SYNCHROTRON RADIATION INSTRUMENTATION – SRI2018*, (2019).
29. J.-F. Ji, H. Guo, Y.-L. Xue, *et al.*, “The new x-ray imaging and biomedical application beamline bl13hb at ssrf,” *Nucl. Sci. Tech.* **34**, 197 (2023).